ALEXANDRIA JOURNAL OF SCIENCE AND TECHNOLOGY

Alexandria Journal of Science and Technology

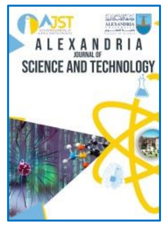

Article

Structural Lineaments Detection using Integrating Remote Sensing and Aeromagnetic Data in Gabal Umm Tinassib and its Surrounding Area, North Eastern Desert, Egypt

Reda Abdu Yousef El-Qassas [1], Mohamed Salaheldin [2,*], Tharwat Abdel Fattah [2], Assran S. M. Assran [1], Magdy Almaghraby [2], Hassan Diab [3], Manal M. Osman [2]

[1] *Exploration Division, Nuclear Materials Authority, Cairo, Egypt*.

[2] *Geology Department, Faculty of Science, Alexandria University, Alexandria, Egypt*.

[3] *Department of Rocks and Geological Mapping, Geological Applications and Mineral Resources Division, National Authority for Remote Sensing and Space Sciences (NARSS), Cairo, Egypt.*

[*] *Correspondence Address:*

Mohamed Salaheldin: Geology Department, Faculty of Science, Alexandria University, Alexandria, Egypt, E.mail address: mohamed.salaheldin1089@gmail.com.

KEYWORDS: Remote Sensing; aeromagnetic; structural lineaments; Gabal Umm Tinassib; Egypt.

Received: March 19, 2024

Accepted: May 23, 2024

Published: June 04, 2024

ABSTRACT: The available remote sensing (RS) and aeromagnetic data were integrated to derive the structural lineaments, both on the surface and in the subsurface, and to determine the locations and depths of causative magnetic bodies, to understand the structures controlling them at Gabal Umm Tinassib and its surrounding area, located in the Egyptian Northern Eastern Desert.

RS data underwent several processing steps to illustrate the main directions of surface lineaments. Various techniques were employed on the aeromagnetic data, including radially averaged power spectrum, high and low-pass, upward continuation filters, analytic signal (AS), source parameter imaging (SPI), and Euler, tilt derivative (TDR), and horizontal gradient magnitude (HGM).

The structural lineaments were identified from the RS maps, they trend in the NE-SW, NW-SSE, and E-W directions, with minor indications in the N-S direction and various others. The power spectrum technique was utilized to get two major average magnetic interfaces at depths of 790 m and 2200 m, which aided in creating of residual and regional aeromagnetic maps. Depth estimates for the tops of causative magnetic bodies were obtained using three different techniques, revealing depth solutions ranging from -3 to -2291 m for AS, -154 m to -2421 m for SPI, and -1 m to -2192 m for Euler. Significant structural lineaments were extracted from various filtered aeromagnetic maps, organized according to magnitude and importance, showing trends in the NW-SE, NE-SW, NNW-SSE, and NNE-SSW directions, with minor trends in the N-S and E-W directions.

1. INTRODCTION

Gabal Umm Tinassib area lies in the North Eastern Desert of Egypt between Latitudes 28° 18′ 1.89″ N & 28° 47′ 1.82″ N and Longitudes 32° 16′ 47.05″ E & 33° 7′ 29.78″ E (**Figure. 1**). The area is characterized by various Terrain differs from rough at the middle and west to smooth at the east (**Figure. 2a**).

RS instruments calculate emitted or reflected radiations in the visible, near-infrared, thermal-infrared, or microwave portions of the electromagnetic spectrum to gather information about the earth's surface from varying distances. This information comprises two types:(1) direct information relay on the properties of the surface materials (composition) and the other (2) indirect spatial information about the surface configuration (geologic structures, landforms, distribution of surface materials, etc.). The magnetic survey reveals magnetic fields generated by various rocks and geological features. It has been extensively utilized across a range of applications, including mapping subsurface lithology and structures such as faults, folds, and shear zones [1, 2, 3, 4].

Online ISSN: 2974-3273

DOI: 10.21608/AJST.2024.277350.1030

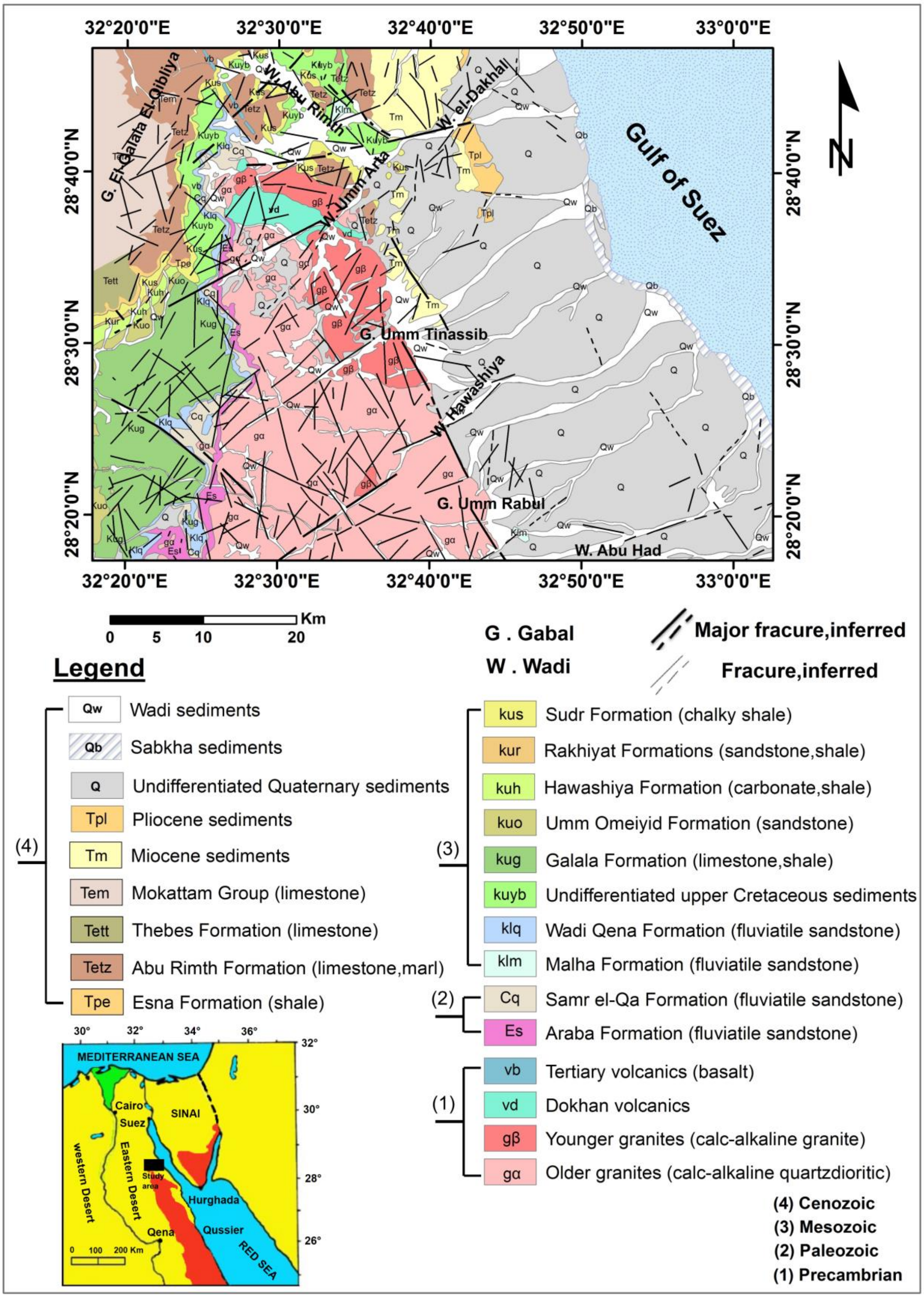

Figure 1. Geologic map of Gabal Umm Tinassib and its surrounding area, North Eastern Desert, Egypt (Reproduced after Conoco Coral and EGPC, 1987), with a location map (inset).

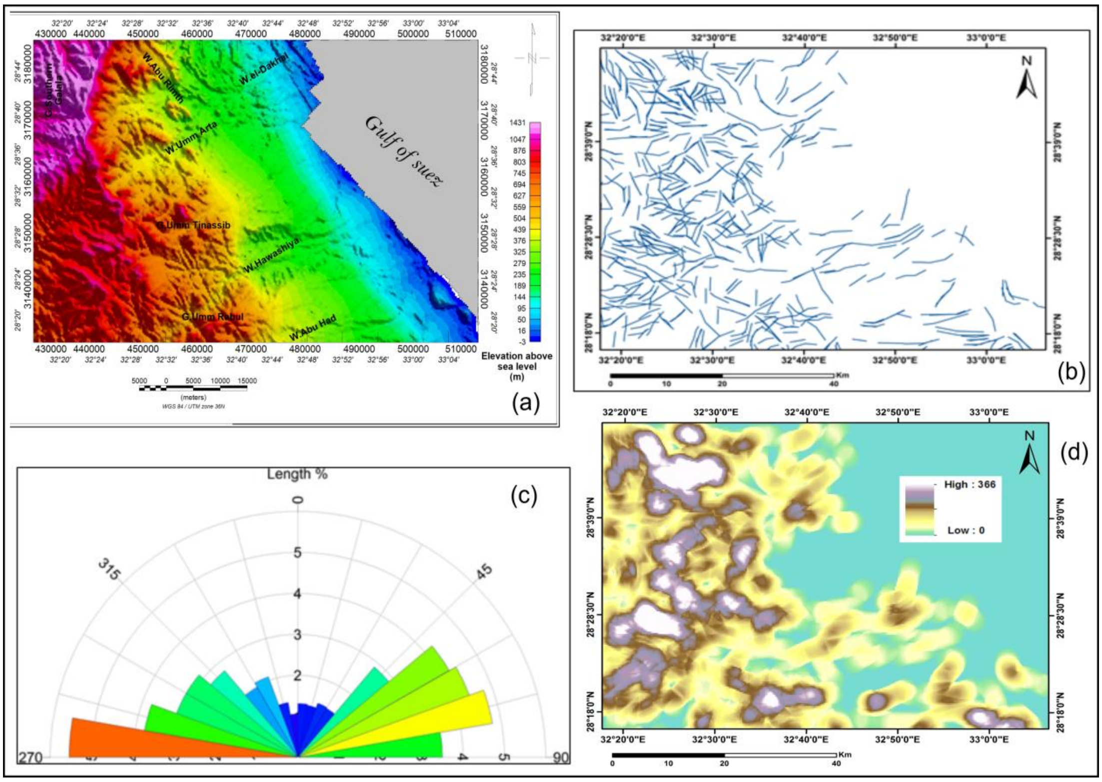

Figure 2. **(a)** Key map showing the elevation above sea level, **(b)** Extracted lineaments, **(c)** Rose diagrams reflecting the main directions of the surficial lineaments and **(d)** Density map of the extracted lineaments, Gabal Umm Tinassib and its surrounding area, North Eastern Desert, Egypt.

Additionally, it serves to identify potential mineralization zones [5, 6, 7, 8]. [10] concluded that the magnetic data detect junction locations and porphyry intrusion. The structural properties may be seen in the intensities and trends represented in aeromagnetic data when evaluating magnetic patterns [11]. Porphyry zones are connected with igneous intrusions in nature and appear as a nearly circular feature. Hydrothermal alteration always enclosed the intrusion showing concentric zones. As the porphyry deposits are the world's dominant source of gold, silver, copper, and other precious metals, investigations into porphyry intrusions hold substantial importance. Magnetic data can characterize geological structures and porphyry intrusions [12].

The objective of this study is to integrate RS and aeromagnetic data to identify both surface and subsurface structural lineaments, determine the locations and depths of causative magnetic bodies, and understand the structures controlling them. Additionally, it aims to follow surface and near-surface geological features to greater depths at Gabal Umm Tinassib and its surrounding area.

2. Geologic Setting

The geology of the researched region is established using the geological map of Benisuef, Egypt, at a 1:500,000 scale [13]. The area has been extensively studied by various researchers [14, 15, 16, 17, 18]. It is covered by a vast diversity of basement and sedimentary rocks extending from Precambrian to Quaternary (**Figure. 1**).

The Precambrian rocks are represented from oldest to youngest by calk-alkaline foliated quartzdioritic to granodioritic (older granites), calk-alkaline deformed granitic (younger granites), Dokhan Volcanics and Tertiary volcanics. These basement complexes are a part of the northern Arabian-Nubian Shield (ANS) and constitute the predominant surface exposures located in the central and southern of the map (**Figure. 1**).

The sedimentary rocks have an age range from Cambrian to Quaternary. They overlay the Precambrian basement rocks, with thick successions represented by Araba, Samr El-Qa, Malha, Wadi Qena, Galala, Um Omeiyid, Hawashiya, Rakhiyat, Sudr, Esna, Rimth, Thebes Formations and Mokattam Group**.** These rocks are obscured by Miocene, Pliocene deposits and Quaternary sediments (Wadi deposits).

Quaternary sediments represent the youngest deposits in the area that consist of Undifferentiated recent coastal deposits, wadi deposits, alluvial fans, raised beaches, gravel, sand, and small localities of clay, silt and evaporates that form Sabkha deposits at the coast line. They occupy the eastern half of the area and form the cover in the main wadis such as Wadi Abu Rimth, Wadi Hawashiya, Wadi Umm Arta, Wadi el-Dakhal and Wadi Umm Rabul (**Figure. 1**).

3. Methodology

RS and aeromagnetic methods were employed to achieve the study's objectives; various image processing techniques have provided high precision in defining structural lineaments within the examined area.

The digital elevation model (DEM) data obtained from the Shuttle Radar Topography Mission (SRTM) were acquired from http://earthexplorer.usgs.gov and processed using PCI Geomatica software. RS data for the studied area were processed for lineament mapping to distinguish surface structural features. Several outputs using the latest version of ArcGIS software including lineaments map, a rose diagram depicting the main trends of surface lineaments and a density map of the obtained lineaments. All are aimed at delineating the surface structure features.

According to [19] the SRTM supervised the creation of specific digital elevation models (DEMs) covering a near-global range from 56° S to 60° N. This effort significantly contributed to Earth's comprehensive high-resolution digital topographic database.

[20] noted that SRTM produces DEM data with a 90 m spatial resolution, facilitating the automated identification of surface lineaments and faults by PCI Geomatica software. The resulting data is further refined through manual intervention to eliminate man-made features.

Western Geophysical Company's Aero-Service Division performed an aeromagnetic survey across a wide portion of Egypt's Northern Eastern Desert. The aeromagnetic survey was done along parallel cross-flight lines pointing northeast-southwest from true north, with azimuths of 45° and 225°. The tie lines were spaced 10 kilometers apart and oriented NW-SE at angles of 135° and 315°. The survey flying average speed was from 220 to 315 km/h and was done at a mean terrain clearance elevation of 120 m. Flight lines were spaced at 1.5 km intervals. A low-sensitivity proton magnetometer (Varian V-85) with 0.1nT was used. The magnetometer is situated in the aircraft's fiberglass tail stringer [21].

The OASIS Montaj processing and mapping system (Geosoft, 2015) was utilized to process the aeromagnetic data, which are represented as contour maps. Various techniques were employed on the aeromagnetic (Reduction to the Northern Magnetic Pole-RTP) data in the study area to identify the locations and depths of high and low magnetic anomaly bodies, as well as the structures controlling them. These techniques encompass radially averaged power spectrum, high and low-pass filters, and upward continuation. Moreover, analytical signal (AS), source parameter imaging (SPI), tilt derivative (TDR), horizontal gradient magnitude (HGM), and Euler deconvolution methods were also employed.

3.1. Radially Averaged Power Spectrum

According to [23] the power spectrum is employed to estimate the average depth of causative bodies. This estimation is derived from the slope of the linear segment within the spectrum graph. Depth is determined as a function of the spectrum's decay within the corresponding frequency interval. The logarithm of the radially averaged energy spectrum plotted against the radial frequency from magnetic data illustrates the decay of this function, representing the depth of the modelled prism.

3.2. High and Low-Pass Filters

[24] defined a high-pass filter as a filter that permits high-frequency signals while eliminating frequencies lower than the designated cut-off frequency. This filter is intended to depict shallow structural bodies. Conversely, a low-pass filter is described as one that removes frequencies higher than the cut-off frequency, aiming to represent deep structural bodies.

3.3. Upward Continuation Technique

The upward continuation technique, as described by [25], is a filtering method that enhances the signal from deeper sources by minimizing or eliminating the effects of shallow sources. This technique involves re-evaluating magnetic anomalies at different elevations, moving farther away from the causative source.

3.4. Analytic Signal Technique.

According to [26], this technique is utilized in frequency or spatial domains, generating high anomalies directly above causative bodies and their edges. [27] established the following equation for calculating the amplitude (A) of the Analytic Signal (AS) of the total magnetic field (M).

$$|A(x,y)| = \left[\left(\frac{dM}{dx}\right)^2 + \left(\frac{dM}{dy}\right)^2 + \left(\frac{dM}{dz}\right)^2 \right]^{1/2} \quad (1)$$

Where; Amplitude of the analytic signal at (x, y) = A (x, y)

Observed magnetic field at (x, y) = M

By calculating the ratio of the total magnetic analytic signal, **A** (**x**, **y**) to the vertical derivative analytic signal of the total magnetic (dA/dz) we obtain the depths of magnetic bodies.

$$D = \left(\frac{A}{\frac{dA}{dZ}} \right) * N \quad (2)$$

Where:

D: Depth of magnetic bodies

N: Structure index

The structures can be detected by the maxima of the analytic signal over the studied area.

3.5. Source Parameter Imaging (SPI).

This method is based on extending the complex analytic signal to calculate magnetic depths. According to [28], the equation for the magnetic field (M) determines the local wavenumber.

$$k = \frac{\frac{d^2M}{dxdz}\frac{dM}{dx} - \frac{d^2M}{dx^2}\frac{dM}{dz}}{\left(\frac{dM}{dx}\right)^2 + \left(\frac{dM}{dz}\right)^2} \quad (3)$$

Then the depth is calculated at the source edge from the reciprocal of the local wave number by

$$Depth_{(x=0)} = \frac{1}{k_{max}} \quad (4)$$

3.6. Tilt derivative technique (TDR).

TDR is a valuable tool used to analyze potential field-gridded data for detecting structural lineaments. [29, 30, 31, 32] calculated the TDR ratio using the following equation

$$\mathrm{TDR} = \tan^{-1}\left(\frac{\mathrm{VDR}}{\mathrm{THDR}}\right) \qquad (5)$$

Where, $\mathrm{VDR}=\frac{dM}{dz}$ is the vertical derivative of the magnetic field (M), and $\mathrm{THDR}=\sqrt{(\frac{dM}{dx})^2 + (\frac{dM}{dy})^2}$ is the total horizontal derivative of the magnetic field (M).

3.7. Horizontal gradient Magnitude (HGM).

The horizontal gradient (HGM) of the magnetic field in a specific direction enhances lateral changes in the magnetic field while attenuates its regional trend along that direction [33]. The derivative will reach a minimum or maximum in areas with higher magnetic susceptibility contrast, thereby emphasizing discontinuities perpendicular to the derivation direction and more precisely delineating faults and structural edges. The HGM method is employed to map linear structures from magnetic data within potential field datasets. [34, 35] established the following equation for this technique

$$\mathrm{HG}(x,y)=\sqrt{(\frac{dM}{dx})^2 + (\frac{dM}{dy})^2} \qquad (6)$$

Where; M magnetic field for (x, y), and HG (x, y): the horizontal gradient magnitude.

3.8. Euler deconvolution.

[36] established this technique for depth estimations and locating several sources within a given area. The Euler equation, defined by [37], is as follows:

$$(x-x_0)\frac{dT}{dx}+(y-y_0)\frac{dT}{dy}+(z-z_0)\frac{dT}{dz} = N(B-T) \qquad (7)$$

Where; (x_0, y_0, z_0): the position of a source whose total field is noticed at any point (x, y, z), T: Total field, N: the degree of homogeneity, interpreted geophysical data as a structural index (SI), and B: The total field background value.

[37] described Structural indices (SI) for some geological structures as SI 0 = Contact, SI 0.5= Thick Step, SI 1= Sill / Dyke, SI 2= Vertical Pipe, and SI 3= Sphere.

4. Results and Discussions

4.1. Remote Sensing (RS) Data

4.1.1. RS Lineament Map

The interpretation of the lineament map derived from RS (**Figure. 2b**) and its rose diagram (**Figure. 2c**) in the examined area represents surface features from the RS perspective. It illustrates significant trends, predominantly in the NE-SW, NW-SSE, and E-W directions, while also indicating minor trends in the N-S direction and various other directions. The rose diagram clarifies these trends by depicting the azimuth distributions of lineament numbers and lengths in the study area (**Figure. 2c**).

4.1.2. Density map

A density map (**Figure. 2d**), constructed from the RS lineaments map (**Figure. 2b**), aims to identify structural density zones. It is evident that the high-density areas, depicted by white colors, reveal zones influenced by tectonic movements along the main shear zone. These high-density zones are indicative of a high level of deformation. [38] and [20] highlighted these high-density zones (often termed weak zones), identified by several authors as favorable channels for the migration of mineralized hydrothermal fluids.

4.2. Aeromagnetic Data

4.2.1. Zonation of the Reduction to the Northern Magnetic Pole (RTP) map

The RTP map (**Figure. 3a**) illustrates the magnetic intensity ranging from -252 nT to 577 nT. The anomalies depicted on the RTP map can be classified into four distinct zones, each exhibiting specific magnetic characteristics. These zones exhibit variations in amplitudes, wavelengths, and trend patterns (**Figure. 3b**).

The first zone (Z1) (pink color) is predominantly situated in the south-central part of the map, extending to various locations in the central, northern, northwestern, and southeastern parts. It comprises notably high positive magnetic anomalies, ranging from 160 nT to 577 nT, and exhibits trends in the NW-SE, N-S, and NE-SW directions.

The second zone (Z2) (red color) encircles the first zone (Z1) and is scattered across certain areas. It is characterized by high positive magnetic anomalies, with amplitudes ranging from 110 nT to 160 nT, displaying trends in the NW-SE, N-S, and NE-SW directions.

The third zone (Z3) (green color) surrounds areas with both high and low values, demonstrating moderate magnetic values ranging from -48 nT to 110 nT, trending primarily in the NW-SE and NE-SW directions.

The fourth zone (Z4) (blue color) is primarily located in the central area, with smaller sections in the southwestern and northeastern parts. This zone comprises low magnetic anomalies, with amplitudes ranging from -252 nT to -48 nT, and trends predominantly in the NW-SE direction, with minor occurrences in the E-W and NE-SW directions.

4.2.2. Radially Averaged Power Spectrum

Upon visually inspecting the two-dimensional power spectrum (**Figure. 4a**), three linear segments have been identified and fitted. The first segment lies at a low frequency with a steep slope, related to the deep causative magnetic sources. Meanwhile, the second and third segments are located at high frequencies with gentle slopes due to relatively shallow sources. The estimated average depths for the regional and two residual sources are 2200 m, 940 m, and 520 m, respectively. The frequency range of 0.00 to 0.06 grid units represents deep sources. Meanwhile, shallow sources have frequency ranges of 0.06 to 0.35 grid units, while shallower magnetic sources have frequency ranges of 0.35 to 1.25 grid units.

4.2.3. High and Low-Pass Filtered Magnetic Maps

The high-pass (residual) magnetic filter holds significant importance in revealing shallow structures on the basement surface or magnetic sources within the sedimentary cover. Examination of the residual aeromagnetic anomalies map (**Figure. 4b**) reveals a sequential pattern of magnetic dipoles characterized by varying amplitudes and frequencies. These anomalies manifest as elongated negative and positive features with relatively high frequencies and low amplitudes, primarily trending in the NNE-SSW and NW-SE directions.

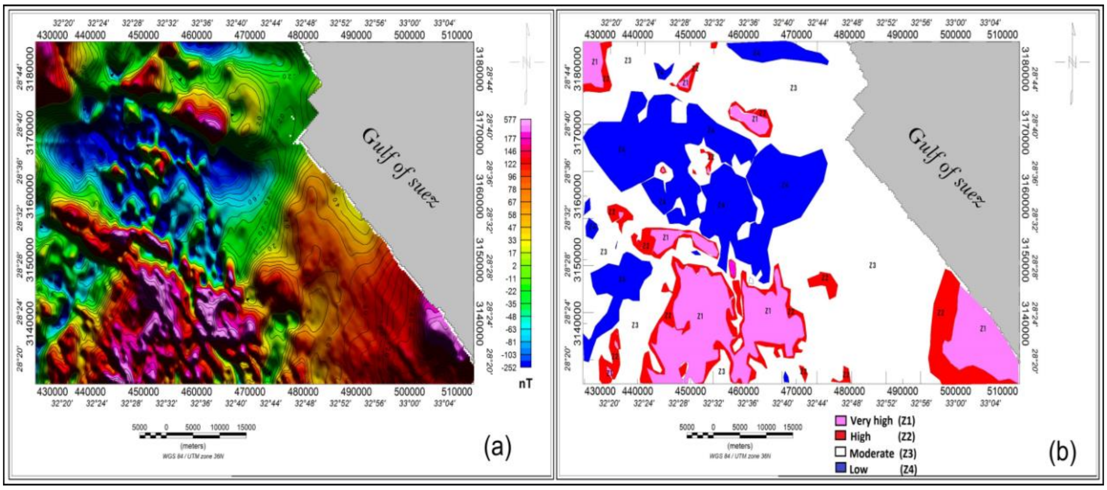

Figure 3. (a) Reduced to the north magnetic pole map (RTP after Aero-service, 1984) and **(b)** magnetic zones as extracted from RTP, Gabal Umm Tinassib and its surrounding area, North Eastern Desert, Egypt.

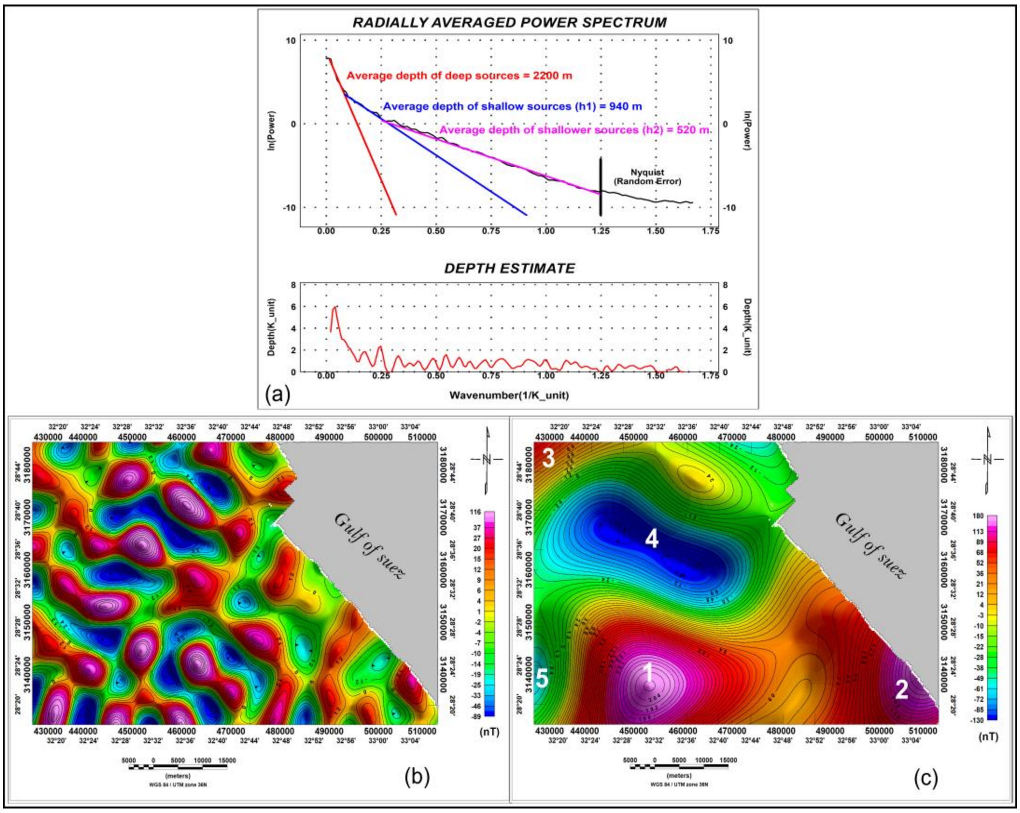

Figure 4. **(a)** Radially averaged power spectrum and depth estimate of the RTP aeromagnetic **(b)** High-pass aeromagnetic map and **(c)** Low-pass aeromagnetic map, Gabal Umm Tinassib and its surrounding area, North Eastern Desert, Egypt.

Conversely, the low-pass (regional) aeromagnetic anomalies map (**Figure. 4c**) displays large, high-amplitude anomalies attributed to deep-seated sources. Upon inspection, two broad positive magnetic anomalies (1 and 2) are evident in the south and southeastern corners, separated by an NNE-SSW fault. Additionally, a high positive magnetic anomaly (3) is observed at the extreme northwest corner, trending in a NW-SE direction. Substantial negative magnetic values (4 and 5) are prevalent in the middle north and southwestern parts, trending in the NW-SE direction. Furthermore, (**Figure. 4c**) shows that the magnetic anomalies within the study area are controlled by two main faults: NNE-SSW and NW-SE.

4.2.4. Upward Continuation Maps.

A sequence of upward continuation filters was applied to the aeromagnetic data at intervals of 500 m, 1000 m, 1500 m, and 2000 m. The upward continued map at 500 m (**Figure. 5a**) reaffirms the features observed in the RTP map (**Figure. 3a**), where both negative and positive magnetic bodies exhibit similar characteristics. This suggests that the majority of the basement rocks responsible for magnetization are either outcropping or buried at shallow depths.

As the upward continuation progresses to levels of 1000 m, 1500 m, and 2000 m (**Figures. 5b, 5c, and 5d**), there is a noticeable trend: with increasing depths, there is a simultaneous attenuation of high-wavenumber anomalies and an increase in broadening.

At 2000 m (**Figure. 5d**), the upward continuation map illustrates a merging of small, isolated positive and negative magnetic anomalies, resulting in larger anomalies or their disappearance. This pattern closely resembles the characteristics of the regional map, estimated to have an average depth of 2200 m.

Also, it agrees well with the regional map in pinpointing the faults that affect the occurrence of magnetic anomalies in the study area (**Figures. 4c and 5d**).

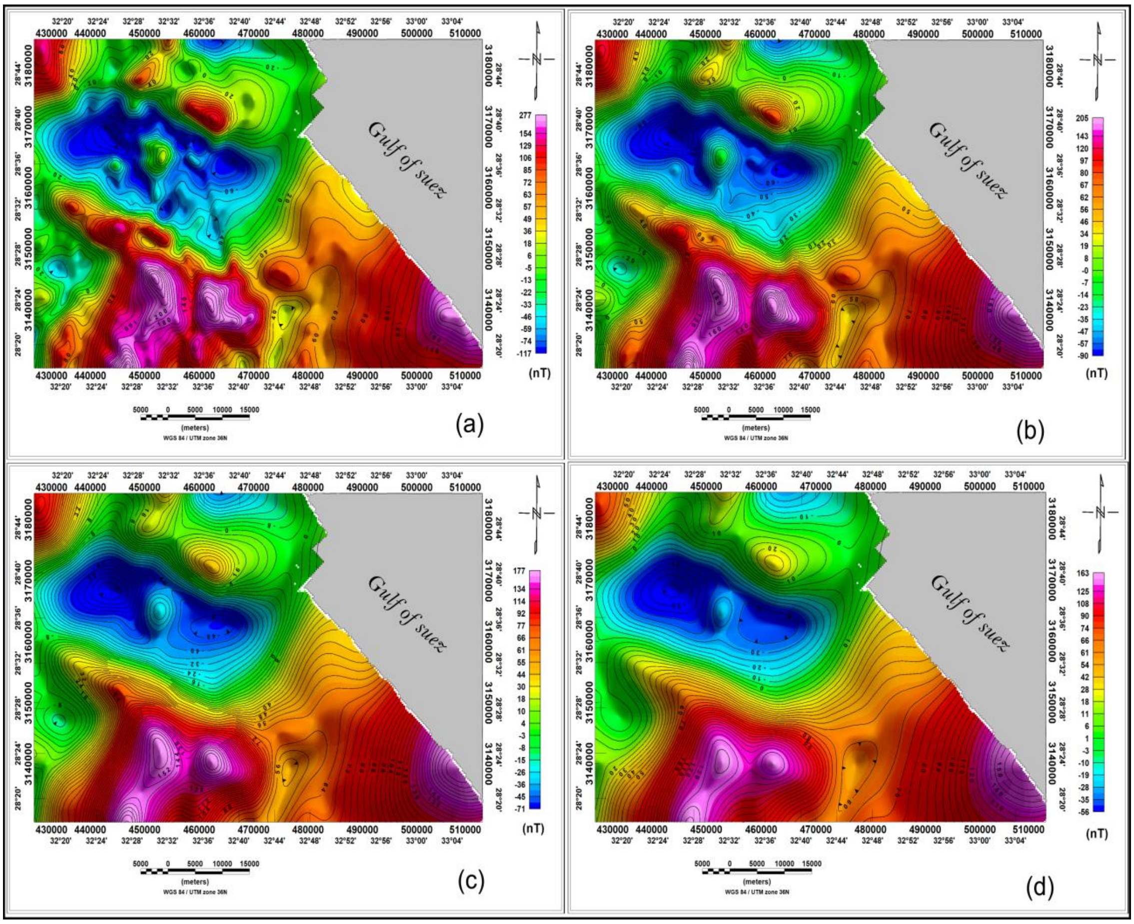

Figure 5. Upward continuation maps at **(a)** 500 m, **(b)** 1000 m, **(c)** 1500 m and **(d)** 2000 m, Gabal Umm Tinassib and its surrounding area, North Eastern Desert, Egypt.

4.2.5. Depth estimation

Depth to the tops of causative magnetic bodies was estimated in the research area using three different techniques; AS, SPI and Euler deconvolution. These techniques operate on the entire grid of data, and the results of the calculated depths are depicted in the corresponding maps (**Figures. 6a, 6b, and 6c**). Analysis of these maps reveals that the depth solutions obtained from the three techniques vary: ranging from -3 to -2291 m for AS, -154 m to -2421 m for SPI, and -1 m to -2192 m for Euler.

The correlation between the surface geology of the study area and the depths derived from the three techniques (**Figures. 6a, 6b, and 6c**) reveals important patterns. Near-surface causative magnetic bodies, from the surface to -200, are predominantly observed in the central and western parts, covered by outcropping basement rock units. In contrast, deep-seated bodies, ranging from 1200 m to more than 2000 m, are situated under a relatively thick cover of sedimentary succession in the eastern and northwestern parts (indicated blue deep-blue coloration).

Magnetic bodies with shallow or intermediate depths (-200 m to -1200 m) are dispersed throughout the area (visible in yellow-green colors), especially over the sedimentary rock units and the wadis (dry-valleys) that traverse the basement rock are related to the thickness of sedimentary cover or irregularities in the depositional surface (the relief of the basement structure).

4.2.6. TDR Technique

The TDR map (**Figure. 7a**) approves the locations of surface causative magnetic bodies, as it centers the high anomaly values directly over them, displaying main trends to the N-S, NE-SW, and NW-SE. Observing the appearance of assumed dykes trending NE-SW and NW-SE, the high negative values indicate the reverse polarity of these dykes.

4.2.7. HGM Technique

The HGM map (**Figure. 7b**) demonstrates that the highest value of the HGM function can map both near-surface and deep-seated magnetic structural features.

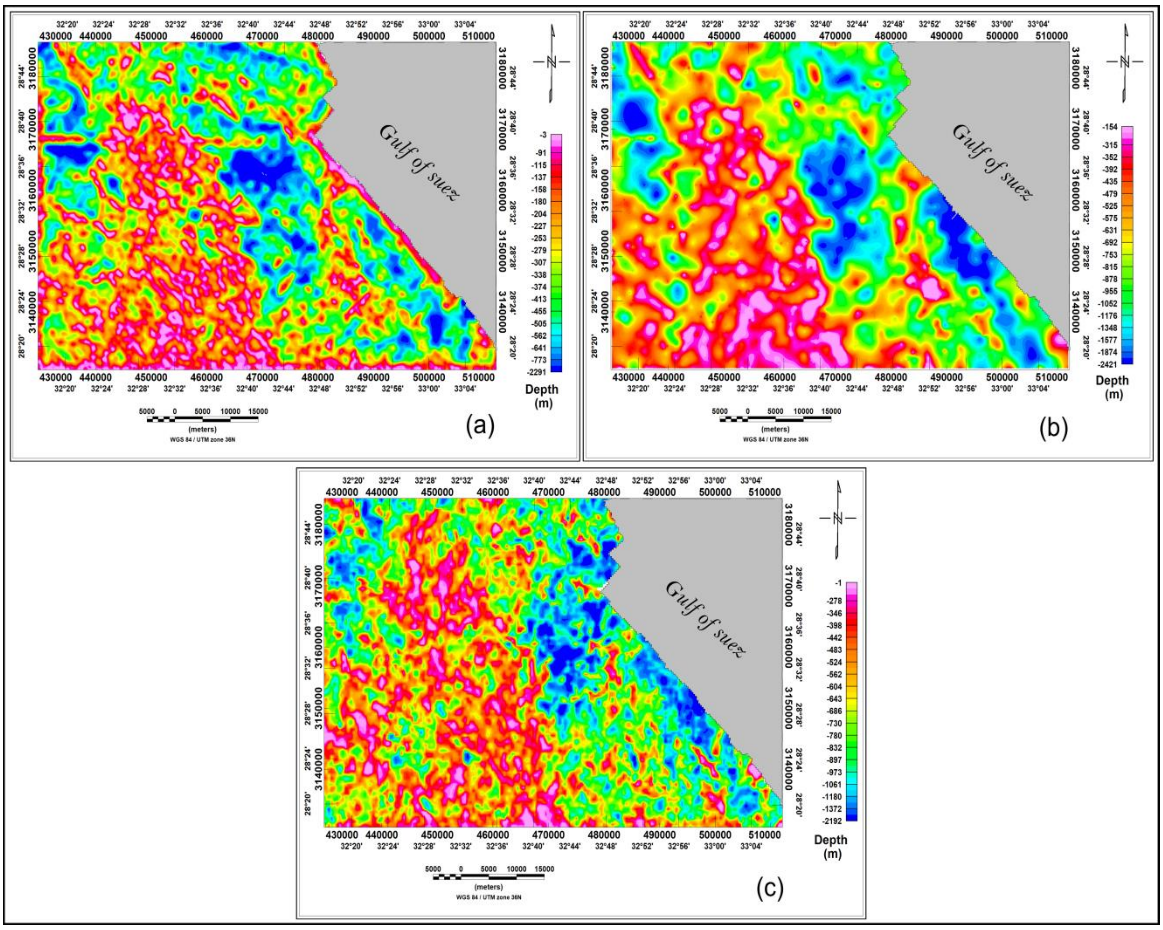

Figure 6. Depth estimation to the top of causative magnetic bodies using **(a)** Analytic Signal (AS), **(b)** Source Parameter Imaging (SPI) and **(c)** Euler deconvolution, Gabal Umm Tinassib and its surrounding area, North Eastern Desert, Egypt.

The variation in the amplitudes of the HGM peaks, linked to the boundaries of the magnetized bodies, may indicate differing depths of these boundaries. HGM peaks generally define lithological contacts trending in the NW-SE, NNW-SSE, and NE-SW directions, with minor trends in the E-W and N-S directions.

4.2.8. Euler deconvolution.

The Euler deconvolution has been extensively used in aeromagnetic interpretation due to its independence from prior knowledge of the source magnetization direction and its absence of reliance on a specific interpretation model [39]. This method was employed to estimate the positions of structural lineaments, primarily responding to data gradients, effectively tracing edges, and defining the depths of the source bodies. The structural index (SI) value identified the source geometry or degree of homogeneity. This technique was applied to the RTP aeromagnetic map of the area of study using two structural indices: SI = 0.0 characterizing faults and contacts, and SI = 1.0 for dykes and sills.

The Euler solutions obtained were visualized as follows: (a) circles of varying colors at their plane positions with corresponding depth, and (b) a 3D gridding map to correlate the obtained results with the AS and SPI results (**Figures. 6a and 6b**). In (**Figures 8a and 8b**), the derived source positions are depicted as circles; the reliable solutions are distinguished by good clustering. Linear sets of solutions indicate traceable faults, contacts, or dykes.

An examination of these maps (**Figure. 8a**) reveals that Euler solutions with SI = 0.0 show robust clustering along linear segments trending in NNW-SSE, N-S, NW-SE, and NE-SW directions, providing depth estimations for these structural lineaments ranging from -218m to -2061m (**Figure. 8a**). Conversely, good clustering with varied depths is observed along the SI = 1 map, aligning with dykes and sills running in the NW-SE, NE-SW, NNW-SSE, and NNE-SSW directions, with depths ranging from -410m to -2232m (**Figure. 8b**).

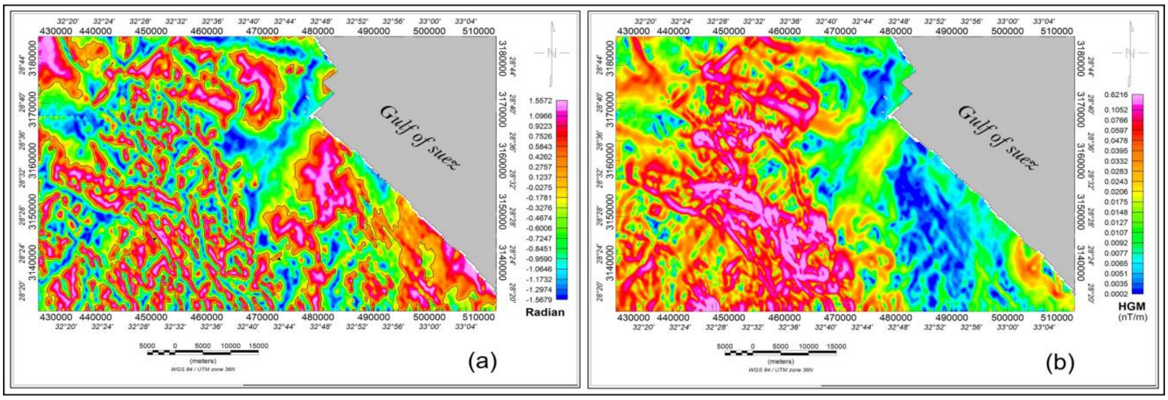

Figure 7. **(a)** Tilt Derivative (TDR) (Continuous black line refer to zero contour values of TDR) and **(b)** Horizontal gradient magnitude (HGM) aeromagnetic maps, Gabal Umm Tinassib and its surrounding area, North Eastern Desert, Egypt.

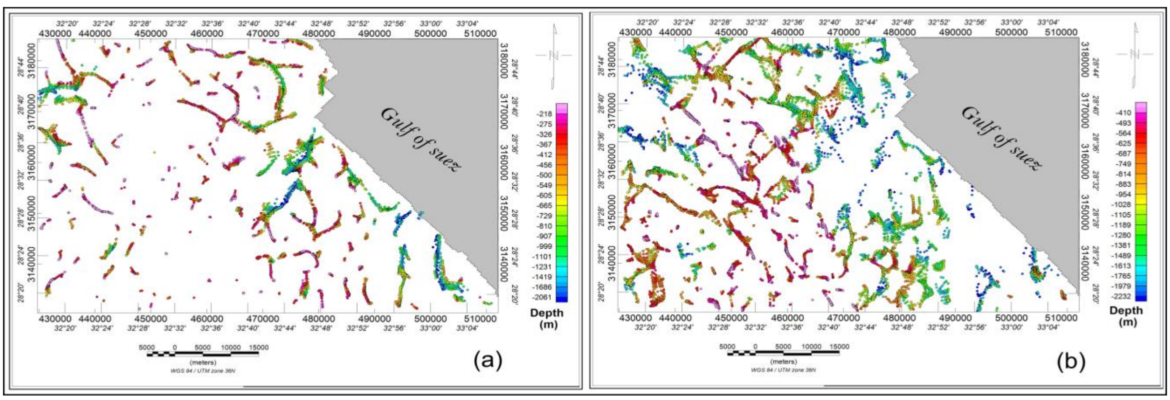

Figure 8. Euler deconvolution solutions with structural index **(a)** 0.0 (SI=0.0) and **(b)** 1.0 (SI=1.0) of the RTP aeromagnetic map, Gabal Umm Tinassib and its surrounding area, North Eastern Desert, Egypt.

4.2.9. Structure lineaments

Rose diagrams were established to demonstrate the azimuth distributions of the number and length percentages of lineaments in the area under investigation. They clarify the directions of the significant structural lineaments resulting from the surface geology, RTP, Regional, and Residual maps (**Figure. 9**).

The important fault systems were clearly observed on the geologic map (**Figure. 9a**) with various geomorphological alignments. The geologic map showed a significant trend in the NE-SW direction, with prevailing trends in the NW-SE and N-S directions, along with other minor trends in all directions.

The RTP rose diagrams (**Figure. 9b**) exhibited a significant trend in the NW-SE direction. The regional rose diagram (**Figure. 9c**) depicted fewer directions, with one major trend in the NW-SE direction.

The residual rose diagram (**Figure. 9d**) generally mirrored the trends observed in the geologic map but with fewer occurrences. The structural features mainly trended in the NE-SW and NW-SE directions. Therefore, these trends are likely the most significant ones in the area of interest.

The study area revealed numerous structural lineaments oriented in the NW-SE, NE-SW, NNW-SSE, and NNE-SSW directions, with minor trends in the N-S and E-W directions. These trends correspond to the Gulf of Suez-Red Sea, Trans-African, Wadi Atalla, Gulf of Aqaba, Meridional (East African), and Mediterranean, respectively [40]. [41] identified the NW-SE structure as one of the Red Sea-related structures. [42] considered the NE-SW trend as an important economic structure in mineral prospecting.

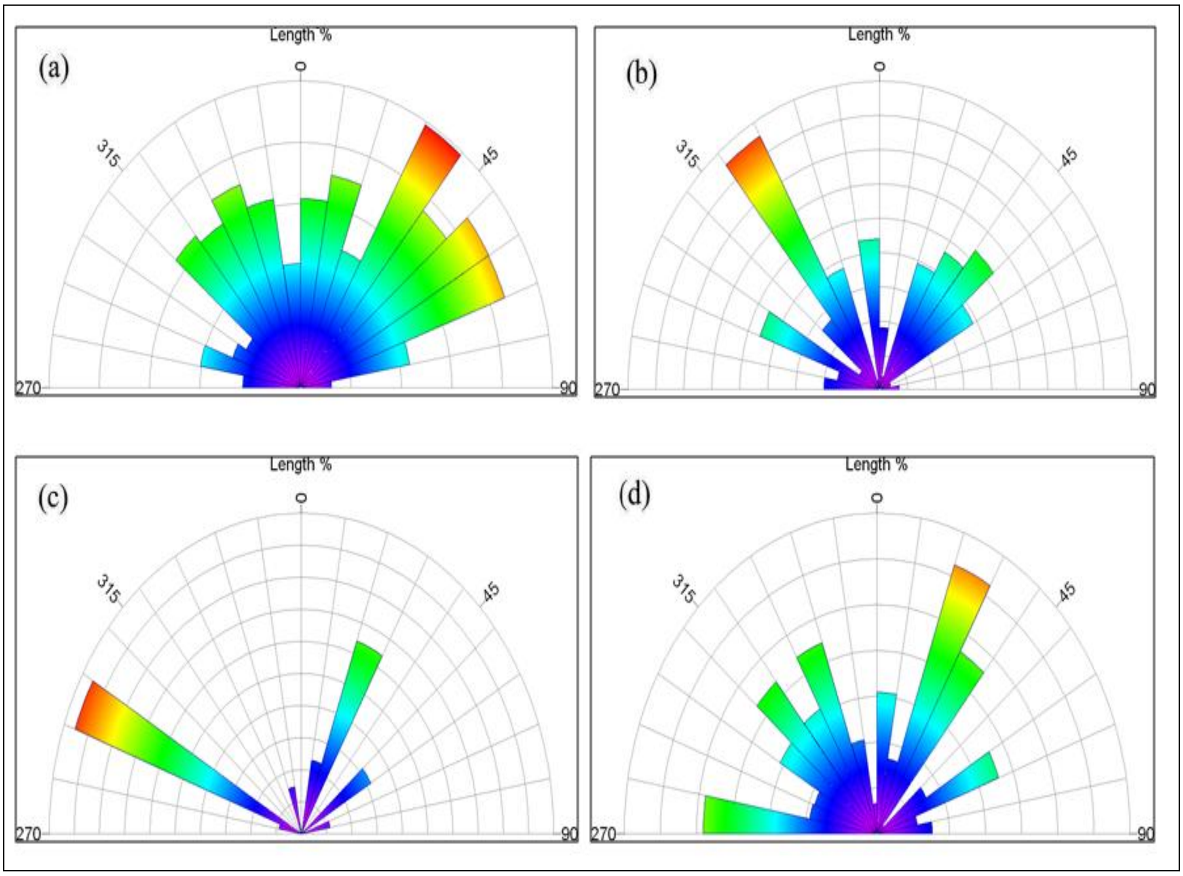

Figure 9. Rose diagrams showing the deduced structural lineaments from **(a)** Geology, **(b)** RTP, **(c)** Low-pass and **(d)** High-pass, Gabal Umm Tinassib and its surrounding area, North Eastern Desert, Egypt.

Conclusions

The analysis of remote sensing (RS) and aeromagnetic data in the study area revealed several significant findings:

Surface structural lineaments were identified from the RS maps, showing trends in the NE-SW, NW-SE, and E-W directions, with minor indications in the N-S direction and various others. A density map derived from the RS lineaments highlighted structural density zones, identified as favourable channels for the migration of mineralized hydrothermal fluids.

The RTP aeromagnetic map was divided into four distinct zones based on variations in amplitudes, wavelengths, and trend patterns, each exhibiting specific magnetic characteristics. The computed power spectrum for the RTP aeromagnetic data indicated average depths of the shallow and deep magnetic sources to be between 790 m and 2200 m, respectively. Depth estimates for the tops of causative magnetic bodies in the study area were obtained using three different techniques: Analytic Signal (AS), Source Parameter Imaging (SPI), and Euler deconvolution, revealing depth solutions ranging from -3 to -2291 m for AS, -154 m to -2421 m for SPI, and -1 m to -2192 m for Euler. Additionally, High and Low-Pass filters, Upward Continuation Filter, and the Tilt Derivative (TDR) technique were applied to the aeromagnetic data to construct corresponding maps, enabling the observation of surface and near-surface geological features at greater depths within the investigated area.

Significant structural lineaments were extracted from various filtered aeromagnetic maps, organized according to magnitude and importance, showing main trends in the directions NW-SE, NE-SW, NNW-SSE and NNE-SSW directions with minor trends in the N-S and E-W directions.

References

[1] Sharma, P. V. Environmental and engineering geophysics, Cambridge University Press, 1997, 475.

[2] Abuelnaga, H.S.; Aboulela, H.; El-Sawy, E.K.; El Qassas, R.A.Y. Detection of structural setting that con-trolling Hammam Faroun area, using aeromagnetic and seismicity data, Gulf of Suez, Egypt. J Afr Earth Sci. 2019, 158, 103560. https://doi.org/10.1016/j.jafrearsci.2019.103560.

[3] Diab, H.; Gabr, S.S.; Abdel Fattah, T.A.; Youssef, M.A.S.; Khalil, I.K. Delineation of the subsurface boundary between the Central and Southern Eastern Desert, Egypt. *The Egyptian Journal of Remote Sensing and Space Sciences.* 2022, 25, 903–918. https://doi.org/10.1016/j.ejrs.2022.09.004.

[4] Abu-Donia, A.M.; El-Qassas, R.A.Y.; Mohamed, A.M.M. Detection of potential hydrocarbon accumulations at Qaret El-Soda area, Western Desert, Egypt, based on airborne geophysical survey data. Exploration Geophysics. 2023, 54, 571-588. https://doi.org/10.1080/08123985.2023.2192864.

[5] Assran, A.S.M.; El Qassas, R.A.Y.; Yousef, M.H.M. Detection of prospective areas for mineralization deposits using image analysis technique of aeromagnetic data around Marsa Alam-Idfu Road, Eastern Desert. Egypt Egyptian J Petrol. 2019, 28(1), 61–69. https://doi.org/10.1016/j.ejpe.2018.11.002.

[6] Aboelkhair, H.; Ibraheem, M.; El-Magd, I.A. Integration of airborne geophysical and ASTER remotely sensed data for delineation and mapping the potential mineralization zones in Hamash area, Southeastern Desert, Egypt. Arab. J. Geosci. 2021, 14, 1–22. https://doi.org/10.1007/S12517-021-07471-Y/FIGURES/20.

[7] Eldosouky, A.M.; El-Qassas R.A.Y.; Pour, A.B.; Mohamed H. Integration of ASTER Satellite Imagery and 3D Inversion of Aeromagnetic Data for Deep Mineral Exploration. Advances in Space Research 2021, 68(9), 3641-3662.
http://dx.doi.org/10.1016/j.asr.2021.07.016.

[8] El-Qassas, R.A.Y.; Ahmed, S.B.; Abd-ElSalam, H.F.; Abu Donia, A.M. Integrating of remote sensing and airborne magnetic data to outline the geologic structural lineaments that controlled mineralization deposits for the area around Gabal El-Niteishat, Central Eastern Desert, Egypt. Geomaterials. 2021, 11, 1–21. https://doi.org/10.4236/gm.2021.111001.

[9] El-Qassas, R.A.Y.; Abu-Donia A.M.; Omar, A.E. Delineation of hydrothermal alteration zones associated with mineral deposits, using remote sensing and airborne geophysics data. A case study: El-Bakriya area, Central Eastern Desert, Egypt. Acta Geodaetica et Geophysica. 2023, 58, 71–107. https://doi.org/10.1007/s40328-023-00405-y.

[10] Holden, E.J.; Fu, S.C.; Kovesi, P.; Dentith, M.; Bourne, B.; Hope, M. Automatic identification of responses from porphyry intrusive systems within magnetic data using image analysis. J. Appl. Geophys. 2011, 74 (4), 255–262.

[11] Gay, S.P.Jr. Fundamental characteristics of aeromagnetic lineaments, their geological significance, and their significance to geology. The New Basement Tectonics American Stereo map Company, Sult Lake City, Utah., 1972, 94.

[12] Eldosouky, A.M.; Abdelkareem, M.; Elkhateeb, S.O. Integration of remote sensing and aeromagnetic data for mapping structural features and hydrothermal alteration zones in Wadi Allaqi area, Southeastern Desert of Egypt. Jour. of Afri. Earth Sci. 2017, 130, 28–37.

[13] Conoco Coral Corporation and the Egyptian General Petroleum Corporation (EGPC). Geological Map of Egypt, Scale 1:500,000, -NH36SW- Beni Suef, Egypt. The Egyptian General Petroleum Corporation, Cairo, Egypt, 1987.

[14] Stern, R.J.; Hedge, C.E. Geochronological and isotopic constraints on Late Precambrian crustal evolution in the Eastern Desert of Egypt. Am J Sci. 1985, 285, 97–127.

[15] Heikal, M.A.; Ahmed, A.M. Some aspects of ignimbritic rhyolites of Gebel Abu Had Dokhan volcanic rocks, Eastern Desert, Egypt. Ann Geo Surv XIII, 1983, 169–184.

[16] Willis, K.M.; Stern, R.J.; Clauer, N. Age and geochemistry of Late Precambrian sediments of the Hammamat series from the Northeastern Desert of Egypt. Precambrian Res. 1988, 42, 173–187.

[17] Eliwa, H.A.; Breitkreuz, C.; Khalaf, I.M.; El-Gameel, K. Depositional styles of Early Ediacaran terrestrial volcanosedimentary succession in Gebel El Urf area, Northeastern Desert, Egypt. J Afr Earth Sci. 2010, 57, 328–344.

[18] Breitkreuz, C.; Eliwa, H.A.; Khalaf, I.M.; El-Gameel, K.; Bühler, B.; Sergeev, S.; Larionov, A.;Murata, M. Neoproterozoic SHRIMP U – Pb zircon ages of silica-rich Dokhan volcanics in the North Eastern Desert, Egypt. Precambrian Res. 2010, 182, 163–174.

[19] Nikolakopoulos, K.G.; Kamaratakis, E.K.; Chrysoulakis, N. SRTM vs ASTER elevation products. Comparison for two regions in crete, Greece. Int. J. Remote Sens. 2006, 27 (21), 4819–4838.

[20] Gabr, S.S.; Diab, H.; Abdel Fattah, T.A.; Sadek, M.F.; Khalil, I.K.; Youssef, M.A.S. Aeromagnetic and Landsat-8 data interpretation for structural and hydrothermal alteration mapping along the Central and Southern Eastern Desert boundary. Egypt. Egypt. J. Remote Sensing Space Sci. 25, 2022, 11–20. https://doi.org/10.1016/j.ejrs.2021.12.00.

[21] Aero-Service. Final Operational Report of airborne magnetic/ radiation survey in the Eastern Desert, Egypt, Conducted for the Egyptian General Petroleum Corporation, Aero- Service Division, Houston, Western Geophysical Co., Taxas, USA, 2019.

[22] Geosoft. Oasis Montaj 8.3.3 mapping and processing system, Geosoft Inc, 2015.

[23] Salako, K.A.; Udensi, E. E. Spectral Depth Analysis of Parts of Upper Benue Trough and Borno Basin, North- East Nigeria, Using Aeromagnetic Data. International Journal of Science and Research (IJSR), India 2013, 2(8), 48–55.

[24] Allen, R.L.; Mills, D.W. Signal Analysis, Time, Frequency, Scale, and Structure, IEEE Press, USA, 2004.

[25] Jacobsen, H.B. A case for upward continuation as a standard separation filter for potential field maps. Geophysics 1987, 52 (8), 1138–1148.

[26] Ansari, A.H.; and Alamdar, K. Reduction to the Pole of Magnetic Anomalies Using Analytic Signal. World Applied Sciences Journal 2009, 7(4), 405-409.

[27] Roest, W.R.; Verhoef, J.; Pilkington, M. Magnetic interpretation using the 3-D analytic signal. Geophysics 1992, 57, 116–125.

[28] Thurston, J.B.; Smith, R.S. Automatic conversion of magnetic data to depth, dip, and susceptibility contrast using the SPI(TM) method: Geophysics, 1997, 62, 807–813.

[29] Miller, H.G.; Singh, V. Potential field tilt – a new concept for location of potential field sources. J Appl Geophys. 1994, 32, 213–217.

[30] Verduzco, B.; Fairhead, J. D.; Green, C.M. New insights into magnetic derivatives for structural mapping, The Leading Edge 2004, 23, 116–119.

[31] Salem, A.; Williams, S.; Fairhead, J.D.; Smith, R.; Ravat, D. Interpretation of magnetic data using tilt-angle derivatives: Geophysics, 2008, 73(1), L1-L10.

[32] Rajaram, M. What's new in interpretation of magnetic data? Geohorizons, 2009, 50.

[33] Blakely, R.J. Potential theory in gravity and magnetic applications, (1stedn) Cambridge Univ. Press, Cambridge, 1995.

[34] Cordell, L.; Grauch, V.J.S. Mapping basement magnetization zones from aeromagnetic data in the San Juan Basin, New Mexico: Society of Exploration Geophysicists, 52nd Annual Meeting, Abstracts and Bibliographies, 1982, 246–247.

[35] Cordell, L.; Grauch, V.J.S. Mapping basement magnetization zones from aeromagnetic data in the San Juan basin, New Mexico, in Hinze, W. J., Ed., The utility of regional gravity and magnetic anomaly maps: Expanded Abstract, Ann. Mtg of Soc. Expl. Geoph. 1985, 181–197.

[36] Thompson, D.T. EULDPH – A new technique for making computer-assisted depth estimates from magnetic data, Geophysics 1982, 47(1), 31–37.

[37] Reid, A.B.; Allsop, J.M.; Granser, H.; Millett, A.J.; Somerton, I.W. Magnetic interpretation in three dimensions using Euler deconvolution, Geophysics 1990, 55, 1, 80–91.

[38] Gupta, R.P. Remote sensing geology, 2nd edn. Springer, Heidelberg, 2003, 655.

[39] Barbosa, V.C.F.; Joso, B.C.; Medelros, W.E. Stability analysis and improvement of structural index estimation in Euler deconvolution. Geophysics 1999, 64(1), 48–60.

[40] Rabie, S.I.; Ammar, A.A. Pattern of the main tectonic trends from remote geophysics, geological structures and satellite imagery, Central Eastern desert. Egyptian Int. J. Remote Sensing 1990, 11(4), 669–683.

[41] Meshref, W.M. The application of magnetic trend analysis to the interpretation of Egyptian tectonics. 9th Ann. Meet. Geol. Soc. Egypt. 1971, 19–21.

[42] Ammar, A.A.; Meleik, M.L.; Fouad, K.M. Tectonic analysis of a sample area, Central Eastern Desert, Egypt, applying aeroradiometric and aeromagnetic survey data, Bull. Fac. Earth Sci. King Abdulaziz University, 1983, 6, 459–482.